



ORIGINAL RESEARCH ARTICLE

Hot Workability and Microstructure Control of Ti6Al4V Alloy

M.S. Dhanya, S. Anoop, Sushant K. Manwatkar, Ravi Ranjan Kumar, Rohit Kumar Gupta, and S.V.S. Narayana Murty

Submitted: 30 July 2023 / Revised: 28 November 2023 / Accepted: 12 January 2024

Titanium alloy Ti6Al4V has been recognized for its high strength-to-weight ratio. Extensive deformation study has been conducted; however, defects like strain-induced porosities, non-uniform microstructure, etc., are observed during thermomechanical processing. So, optimization of thermomechanical processing parameters is highly essential to avoid the recurrence of these kinds of defects. Characterization of defects noticed in hot-rolled ring sample was carried out and a detailed deformation study has been conducted to understand the generation of such defects to avoid their occurrence. The study has been conducted in the temperature range of 800-1050 °C and strain rate of 0.001 to 10 s⁻¹ using a Gleeble 3800 thermomechanical simulator. Microstructural mapping of the deformed Ti6Al4V is carried out. Workability by hot deformation is explained through processing maps. As per the efficiency of power dissipation maps, the maximum efficiency of 65-70 % is obtained in the temperature range of 825-900 °C and strain rate 10⁻³ to 10^{-2.5} s⁻¹ up to 0.4 strains. Arrhenius equations are used to calculate the activation energy of hot deformation and an average of 620.62 kJ/mol was obtained for the temperature range of 750-950 °C. Prediction capability of constitutive models like the modified Johnson–Cook (m-JC) model and artificial neural network (ANN) was verified for deformation behavior. ANN model is found to give the best fit with an absolute average error (AARE) of 0.0417 and correlation coefficient (*R*) 0.9985. Hot rolling was also conducted at different temperatures of 800-950 °C in the intervals of 50 °C up to 50 % reduction. Microstructure obtained through hot compression and hot rolling is discussed. Specimen hot compressed at 800 °C and strain rates of 0.001, 0.01, 0.1, 1 and 10 s⁻¹ showed strain-induced porosities along the grain boundaries. Similarly, hot-rolled samples at 800 °C showed the presence of strain-induced porosities.

Keywords hot workability, processing maps, Ti6Al4V, thermomechanical processing

1. Introduction

Titanium alloys are characterized by their excellent properties like high strength-to-weight ratio, good fatigue strength, formability and excellent corrosion resistance and capacity to withstand a wide range of temperatures (Ref 1). Due to the combination of these properties, Ti alloys are extensively used in aerospace applications. The high melting point of Ti alloys along with good machinability and weldability led to the development and use of Ti alloys for various aerospace structural components. Among the Ti alloys, Ti6Al4V is the most important, called the workhorse of the titanium industry. It is an $\alpha + \beta$ alloy with a mixture of predominant α phase with hexagonal close-packed structure (hcp) and transformed β phase with body-centered cubic (bcc) structure. This alloy contains 6 wt.% aluminum (improves strength and hardness)

which stabilizes α phase and 4 wt.% vanadium which stabilizes the β phase (improves ductility and mechanical properties).

Hot working is essential for the processing and fabrication of components for different structural applications. A series of thermomechanical processing steps are involved in the transformation of as cast microstructure to the worked microstructure. Fabrication of structural components from the alloy by thermomechanical processing may induce defects like strain-induced porosities, flow localization, etc., in the material which may adversely affect the performance of the component. Normally alloys are deformed at low temperatures in the hot working regime to get the desired microstructure. However, the hot workability of titanium alloys decreases with decrease in temperature (Ref 2-4). The thermomechanical processing variables (temperature and strain rates) should be controlled, such that the desired microstructure without any defect is obtained to achieve the desired mechanical properties. The microstructural change depends on the amount of prior deformation and working temperature and the mode of deformation (Ref 5, 6). T. Seshacharyulu et al. conducted hot working studies of commercial grade Ti6Al4V with lamellar starting structure and observed that the material exhibited cracking at prior beta grain boundaries at lower strain rates < 10⁻¹ s⁻¹ due to incompatibility of deformation behavior of α and β phases. The material also exhibited flow instability and intense flow localization manifested by adiabatic shear bands and lamellae kinking at very high strain rates > 1 s⁻¹ (Ref 7).

The response of Ti6Al4V during hot compression at different elevated temperatures and strain rates was extensively

M.S. Dhanya, S. Anoop, Sushant K. Manwatkar, and Rohit Kumar Gupta, Vikram Sarabhai Space Centre, Thiruvananthapuram 695022, India; Ravi Ranjan Kumar and S.V.S. Narayana Murty, Liquid Propulsion Systems Centre, Thiruvananthapuram 695022, India. Contact e-mail: dhanyarajesh130@gmail.com.

studied using several approaches to predict the flow curves of Ti6Al4V. Zener–Holloman parameter has been used by researchers to identify the deformation mechanisms in α and $\alpha + \beta$ regions (Ref 8, 9). Activation energies for Ti6Al4V at low- and high-temperature regimes were estimated for predicting the hot deformation behavior and establishing the mechanisms in α and $\alpha + \beta$ phase microstructures (Ref 10, 11). Souza et al. described the deformation behavior of Ti6Al4V alloy with equiaxed and martensitic initial microstructures in the $\alpha + \beta$ phase region using a microstructural-based Estrin Mecking (EM) + Avrami model (Ref 12). Lin et al. investigated the deformation behavior of Ti6Al4V alloy during the isothermal compression and hot tensile experiments. Their studies based on probability densities of parameters in the constitutive model revealed variation of parameters similar to normal distribution. A constitutive model was suggested utilizing the constitutive parameters corresponding to maximum probability density (Ref 13, 14).

However, problems related to microdefects on the thermo-mechanical processed alloy components are still to be reported and it becomes more critical when the final component thickness is small (Ref 15).

The development of physical models simulating the effects of deformation mechanisms involved during the deformation of the alloys is essential for interpretation of the deformation behavior at different temperatures and strain rates. The empirical models, such as modified Johnson–Cook and strain-compensated Arrhenius equations, are explored in the present work due to their computational efficiency and ease of integration into finite element analysis (FEA) and the same has been used in the present work. Similarly, artificial neural network (ANN) became an important method for predicting hot deformation behavior with the advent of several computational algorithms. Murat Mert Uz et al. employed ANN to study the flow stress behavior of tensile tested Ti6Al4V from 500–800 °C and suggested it as the more suitable approach for the interpretation of flow stress behavior (Ref 16). We have used ANN for flow stress behavior investigation of the alloy from 800 to 1050 °C.

Though Ti alloy Ti6Al4V has been extensively studied for thermomechanical behavior, defects are still observed in the hot-worked material (Ref 15). Available literature could partly provide reasons for such defect generation in extensively worked material. Hence, to bring out a better understanding of such defect formation, a systematic study on the hot workability of Ti6Al4V is conducted and a microstructural comparison to different hot working conditions addressing the generation of strain-induced porosity (SIP) in addition to other instability situations is carried out. The flow stress data obtained as a function of temperature, strain rate and strain are used to develop the processing maps. Further, hot rolling was also carried out at different temperatures in another set of samples from the same batch of material to know the generation of such defects in the rolling process.

2. Experimental

Vacuum arc remelted (VAR) and cogged disk of Ti6Al4V (Fig. 1) of 600 mm diameter is the initial material for the fabrication of rings/forgings for pressure vessels. Some microstructural defects were noticed in the hot-worked

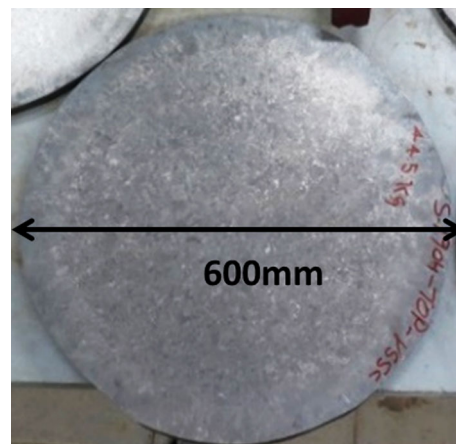


Fig. 1 Vacuum arc remelted (VAR) and cogged disk of Ti6Al4V

Ti6Al4V material. The chemical composition of the alloy is Ti-5.4 Al-4.2 V-0.04 Fe-0.16 O-0.02 N-0.003 H. The specimens with defects were sectioned, metallographically polished and etched with Kroll's reagent. Open defects observed in the machined ring were analyzed. Careful polishing was carried out on the samples with embedded defects to reveal them for metallographic examination. The metallographic observations were carried out using Olympus GX71 optical microscope. The specimens were analyzed using a Carl Zeiss EVO-50 scanning electron microscope (SEM). The open surface defects (revealed after machining) were named OP-1 and OP-2 and embedded defects (opened through polishing) were named as E-1, E-2 and E-3 as shown in Fig. 2. The details of these defects are provided in Table 1. Further to understand and simulate the generation of such defects, a detailed systematic thermomechanical study was conducted.

As a part of the detailed thermomechanical processing evaluation of the Ti6Al4V alloy, hot compression specimens of dimensions 15mmX10mm were prepared from the initial forged ingot (just after the initial breakdown of the ingot) by EDM machining. The compression specimens were undergone isothermal hot deformation test in a Gleeble 3800 thermomechanical simulator in the temperature range of 800–1050 °C at 50 °C intervals and in the strain rate range of 10^{-3} – 10 s $^{-1}$ at tenfold increase intervals. The specimens were heated to the specified temperatures inside the thermomechanical simulator with a heating rate of 10 °C/min and held for five minutes for uniform distribution of temperature throughout the specimen followed by compression of the specimen up to 50% height reduction at constant strain rate. The specimens were cooled by water quenching after hot compression. Graphite foil was inserted in between the specimen ends and platen during the hot compression experiments. The barreling coefficient was < 1.1 for all test conditions, and hence, friction factor was not been considered in calculation (Ref 17).

The schematic representation of hot deformation studies of Ti6Al4V alloy at different temperatures and strain rates is provided in Fig. 3.

The compression-tested specimens (Fig. 4) were sectioned vertically into two halves. Each half piece of different temperature and strain rate conditions was mounted, polished and etched metallographically to reveal the microstructure which was investigated by using an Olympus metallurgical microscope.

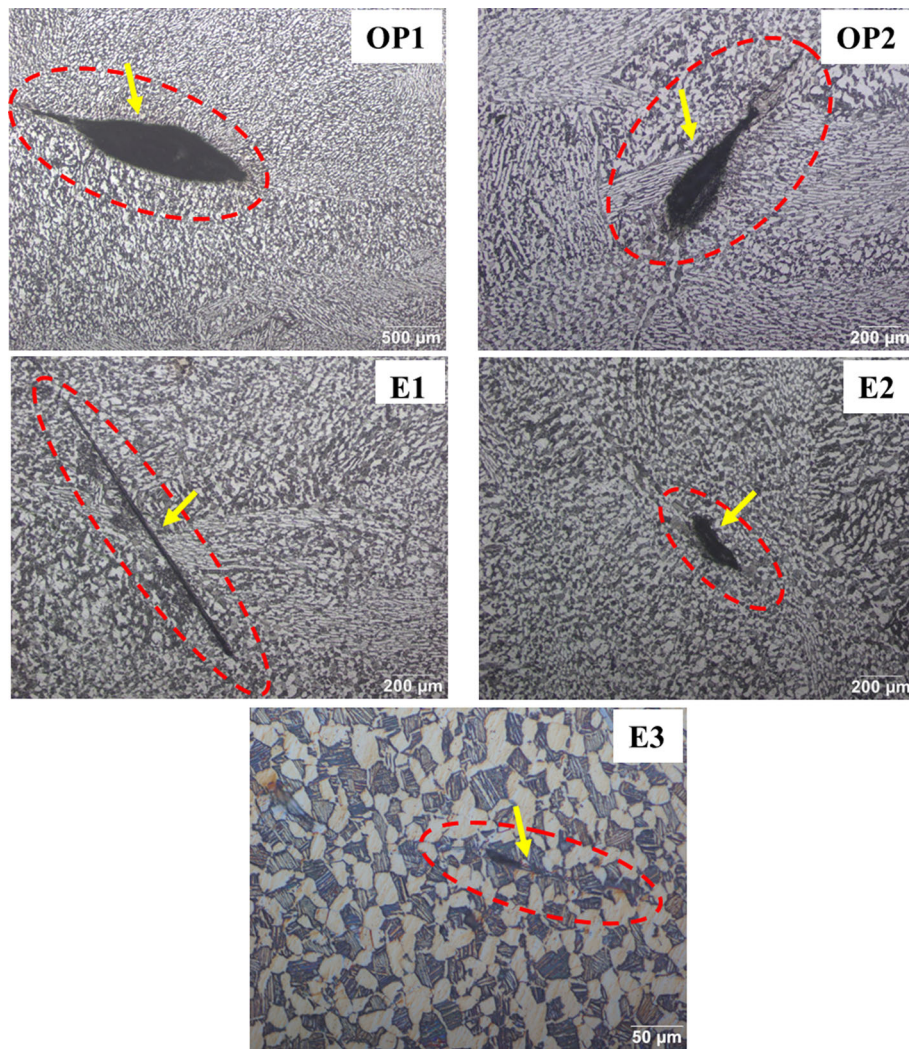


Fig. 2 Optical microstructure showing strain-induced porosities along the prior beta grain boundaries (OP1, OP2), local variation in microstructure and embedded defects opened to surface along the prior beta grain boundaries (E1, E2 & E3)

Table 1 Details of the open and embedded defects observed

Sl. No	Defect type	Length, μm	Width, μm
1.	OP1	1412	267
2.	OP2	424	167
3.	E1	815	87
4.	E2	208	56
5.	E3	270	42

Stress–strain data were evaluated and microstructural mapping was conducted for all test conditions. Cross section of specimens was analyzed under scanning electron microscope (SEM) for the presence of any defects after hot compression. The flow stress data obtained as a function of temperature, strain rate and strain were used to develop the processing maps which are interpreted based on microstructural observations. In the processing maps and instability contour maps, a graphical representation of the response of the material to different deformation conditions was developed to determine the best

deformation conditions and identify unstable regions of hot working. Constitutive equation models like the modified Johnson–Cook (m-JC) model and artificial neural network (ANN) were developed based on the flow stress data and their prediction capability is compared. The deformation behavior was interpreted based on these simulation models.

Further, as a part of large strain rolling studies, Ti6Al4V specimens were separately hot-rolled unidirectional at different temperatures of 850, 900 and 950 °C in two steps up to 50% reduction. The rolling was performed in two passes and the material was air-cooled after the final rolling process. The microstructural analysis of metallographically prepared specimens after hot rolling was conducted. Tensile specimens were fabricated out of these hot-rolled sheets and mechanically tested in an Instron UTM machine. The fracture surface of the tensile samples was analyzed by SEM. EBSD analysis was carried out on sectioned and vibratory polished hot-compressed specimens using a Carl Zeiss Gemini560 scanning electron microscope with an Oxford EBSD detector. The data were analyzed using AZTEC INCA & AZTEC crystal software.

3. Results and Discussion

3.1 Surface and Embedded Defects on Hot Worked Component

Open surface defects (Open-OP) and embedded defects (E) were noticed in the primarily worked Ti6Al4V disk during the fluorescent penetrant test after final machining for the fabrication of propellant tank. During microstructural analysis, strain-induced porosities along the prior beta grain boundaries with variation in microstructure and some embedded defects were

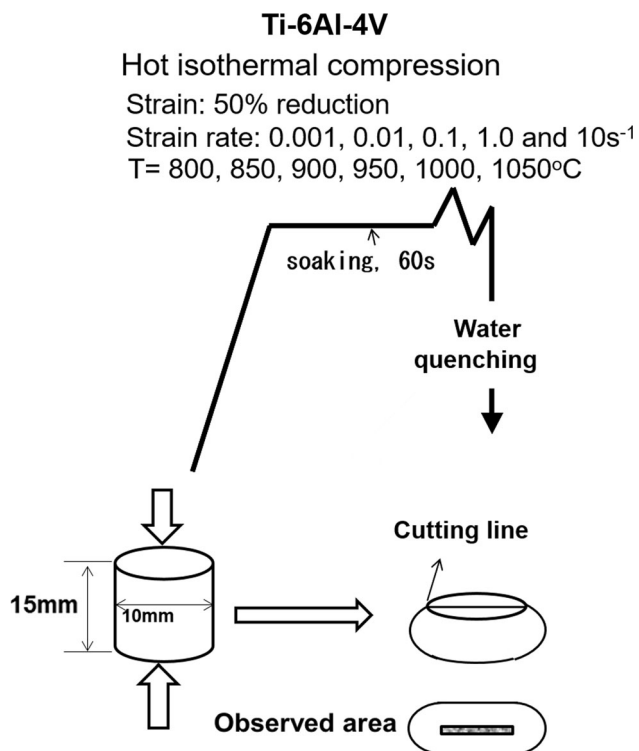


Fig. 3 Schematic representation of hot deformation of Ti6Al4V at different temperatures and strain rates

observed locally in Ti6Al4V rings as shown in Fig. 2. The measurements of these defects are provided in Table 1.

The initial microstructure of the VAR ingot of Ti6Al4V is provided in Fig. 5. The coarse acicular $\alpha + \beta$ microstructure was revealed in the ingot disk. The white plates in the microstructure are alpha and the dark region between them is beta. Normally equiaxed or bimodal microstructure is preferred for this alloy for most of the structural applications due to improved ductility (Ref 18). The α to β transition temperature of this alloy is 980 °C (Ref 19).

The origin of these defects could be due to variations in melt-related or thermomechanical processing-related parameters (Ref 19). Melt-related deviations need to be controlled during electrode preparation/vacuum arc remelting (VAR). The thermomechanical processing-related issues are to be solved by controlling thermomechanical processing parameters like temperature and strain rate. Simulation of defects through hot compression test and hot rolling is presented and discussed in subsequent sections.

3.2 Stress-strain Behavior

The stress-strain curves of Ti6Al4V alloy obtained from the Gleeble isothermal hot compression test of Ti6Al4V at different temperatures of 800, 850, 900 and 950 °C and at different strain rates of 0.001, 0.01, 0.1, 1 & 10 are provided in Fig. 6(a), (b), (c) and (d).

The curves indicate that the flow stress is sensitive to hot deformation temperature and applied strain rates. It shows a trend of reduction in peak stress as the strain rates reduce (from 0.001 s⁻¹ to 10 s⁻¹) for a particular deformation temperature. Flow stress decreases with an increase in temperature for a particular strain rate. During the hot deformation, both strain hardening and flow softening occur simultaneously in the material and whichever dominates will determine the flow stress behavior of the alloy. At the initial stages of the deformation of the material, the strain hardening is very high due to the increase in dislocation density, and hence, the flow stress increases drastically due to the dislocation pile-ups. Subsequently, on increasing the strain further, the flow curves exhibited a continuous flow softening behavior after the peak

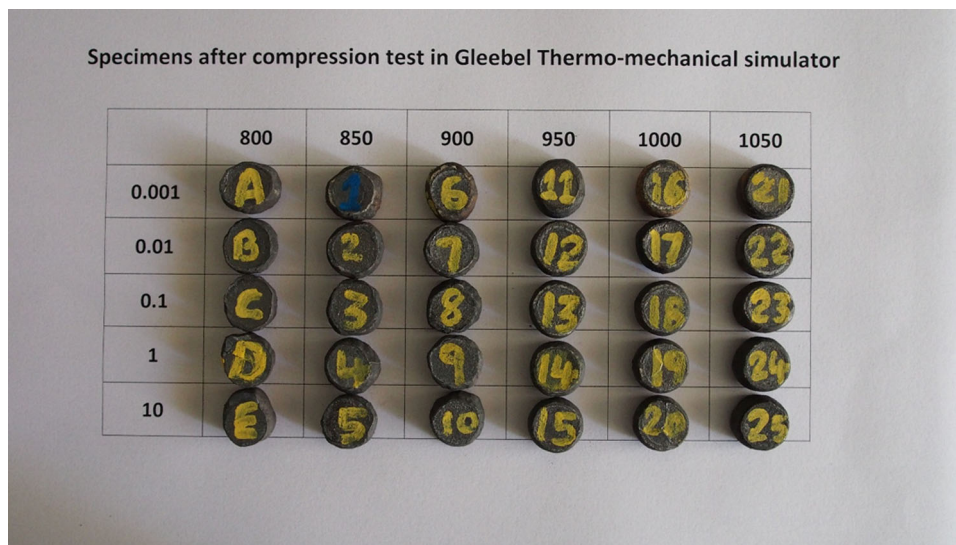


Fig. 4 Specimens hot compressed in Gleeble thermomechanical simulator

stress in all the test conditions. This variation in the exhibited flow behavior with changes in deformation temperature and strain rate is mainly because of dynamic recrystallization (DRX) and dynamic recovery (DRV). Stress–strain curves exhibited steady-state flow indicative of dynamic recrystallization at lower strain rates of 0.01 and 0.001 s^{-1} . At low strain

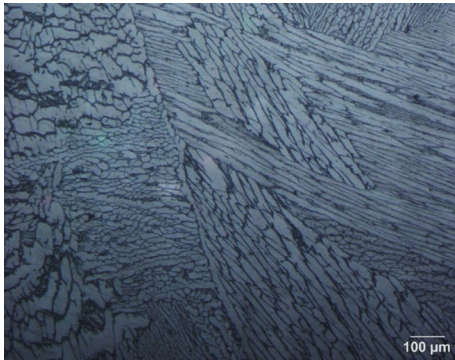


Fig. 5 Initial microstructure of Ti6Al4V VAR melted and cogged disk

rate, the deformation is happening slowly, such that sufficient time is available for DRX.

The initial strain hardening at a lower strain rate is due to the accumulation of dislocations which hinders further dislocation movement. At higher strain rates of 1 and 10 s^{-1} , strain hardening dominates over flow softening and results in high dislocation density and flow stress. Flow stress data of Ti6Al4V at different temperatures, strain rates and strains (corrected for adiabatic temperature rise) are provided in Table 2.

T. Seshacharyulu et al. reported super plasticity behavior in the temperature range of 750-950 °C at lower strain rates and revealed flow instabilities at higher strain rates (Ref 20). At a higher strain rate 10 s^{-1} , fluctuation in flow stress with strain is observed in the stress strain curve indicating the presence of localized unstable plastic flow in the material.

3.3 Microstructural Mapping

The microstructures of all the sectioned hot-compressed specimens were analyzed under a metallurgical microscope to study the variation in microstructure with variation in test conditions and the presence of any defects in the microstructure. Figure 7(a), (b), (c), (d) and (e) shows optical microstructures of Ti6Al4V hot-compressed specimen of 800 °C and

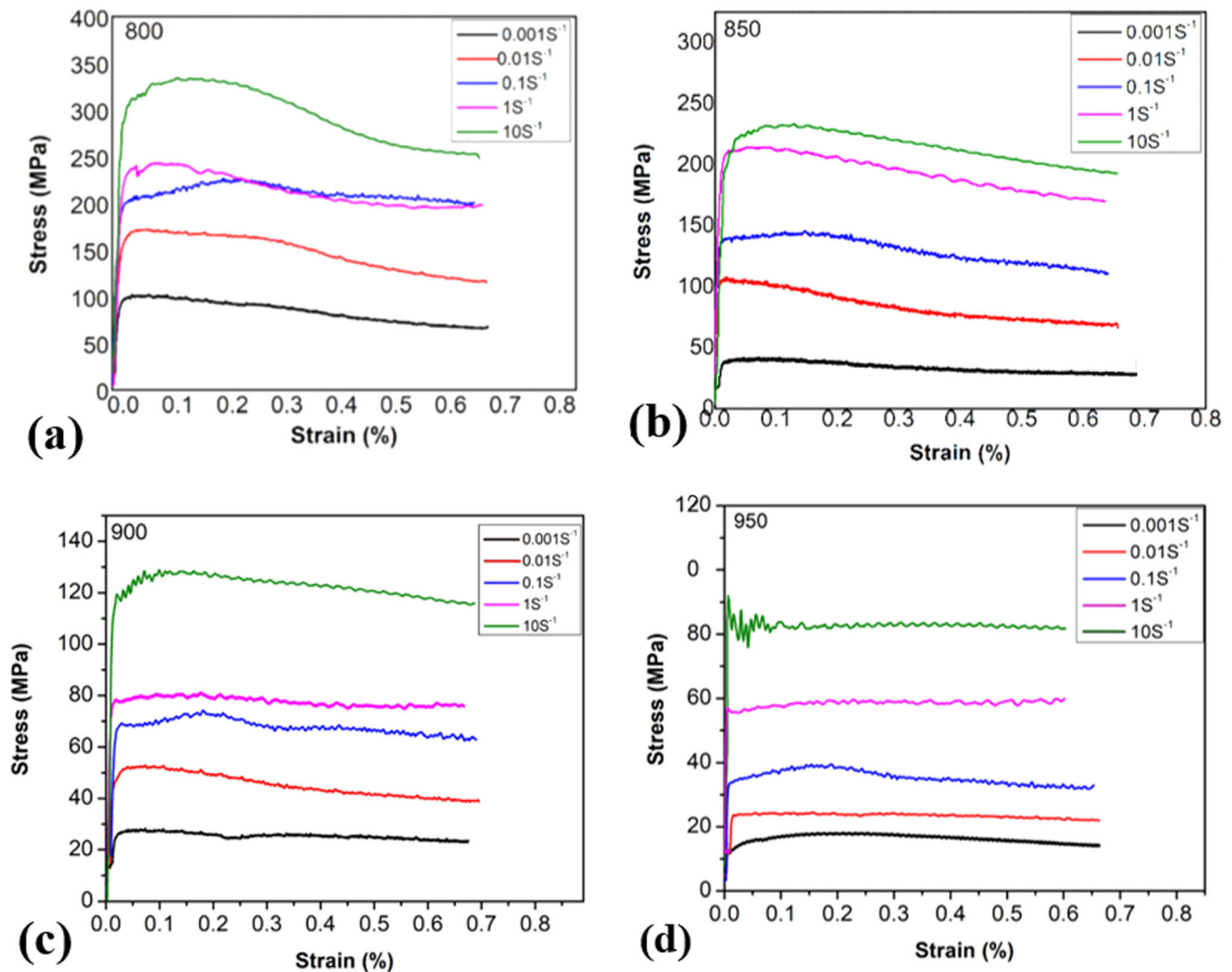


Fig. 6 Stress–strain curves at different deformation temperatures in the strain rate of 0.001-10 s^{-1} (a) 800 °C, (b) 850 °C, (c) 900 °C, (d) 950 °C

Table 2 Flow stress (MPa) at different temperatures, strain rates and strains

Strain	Strain rate, s ⁻¹	Flow stress in MPa at different temperatures (°C)					
		800	850	900	950	1000	1050
0.1		800	850	900	950	1000	1050
	0.001	100.4961	40.3423	27.6094	16.8995	13.17405	12.35985
	0.01	169.8932	100.7561	52.0894	24.02065	17.53297	10.48479
	0.1	211.4081	142.4699	69.60242	37.41702	30.03828	23.36559
	1	241.5828	212.0137	80.0592	57.51607	48.85983	42.11265
	10	329.6961	230.9542	127.5677	83.52855	75.05895	67.34484
0.2		800	850	900	950	1000	1050
	0.001	93.59844	37.6458	25.8094	17.84843	13.12281	12.72852
	0.01	165.6391	90.8289	49.1415	23.85583	17.901	11.74436
	0.1	224.0955	140.7132	72.4183	38.5371	30.23306	23.94898
	1	232.4829	206.3377	78.9752	58.59089	50.35095	44.63449
	10	330.2722	227.9097	126.8683	82.77442	77.17224	69.96433
0.3		800	850	900	950	1000	1050
	0.001	89.13	33.7891	25.4652	17.43799	12.57559	12.88661
	0.01	159.7572	82.3032	45.7029	24.19472	17.62875	12.58269
	0.1	215.84	131.6029	68.132	35.57898	30.62008	24.98988
	1	218.9157	196.6526	77.3678	58.81089	51.50723	46.08253
	10	313.2417	219.862	124.4565	82.86048	79.10034	72.06817
0.4		800	850	900	950	1000	1050
	0.001	80.557	31.6296	25.3745	16.6181	12.12403	12.57077
	0.01	143.3026	77.0613	43.2772	23.687	16.9525	12.7204
	0.1	208.6014	123.2946	67.3885	34.7849	31.43873	25.15868
	1	204.433	187.2952	76.5918	58.5055	52.59096	47.70229
	10	286.4904	211.8174	122.647	82.7017	79.63414	73.86947
0.5		800	850	900	950	1000	1050
	0.001	74.3042	29.6839	24.9599	15.6462	11.24636	12.191
	0.01	130.4389	72.9953	41.5387	23.2725	16.38147	12.79877
	0.1	206.3623	199.202	66.364	33.2444	31.93126	25.453
	1	197.7965	178.5384	75.7899	59.1808	55.27625	48.483
	10	265.4468	203.087	120.6001	82.2677	81.84201	74.7004

strain rates of 0.001, 0.01, 0.1, 1 and 10 s⁻¹ showing strain-induced porosities along the grain boundaries. The SEM image showing the enlarged view of the defect is provided in Fig. 7(f) and (g). Homogeneous material flow was observed without the presence of any defects under all other test conditions except the sample deformed at 800 °C. The evolution of strain-induced porosities during the hot working of Ti6Al4V is reported and found that this plasticity-controlled cavity coalescence normally occurs at low temperatures (Ref 20-22). The detailed microstructural mapping of all the test conditions is

provided in Fig. 8. The microstructure of isothermally compressed specimens at 800 and 850 °C revealed slightly elongated alpha in transformed beta at all strain rates. Upon increasing the temperature beyond 900 °C, material started to transform to beta matrix along with alpha. At temperatures > 950 °C, the deformation of the material happens fully at the beta regime. Microstructures of specimens hot pressed to higher temperatures > 950 °C show that the equiaxed $\alpha - \beta$ microstructure has been changed to Widmanstatten structure. Further, research shows that microstructure at different condi-

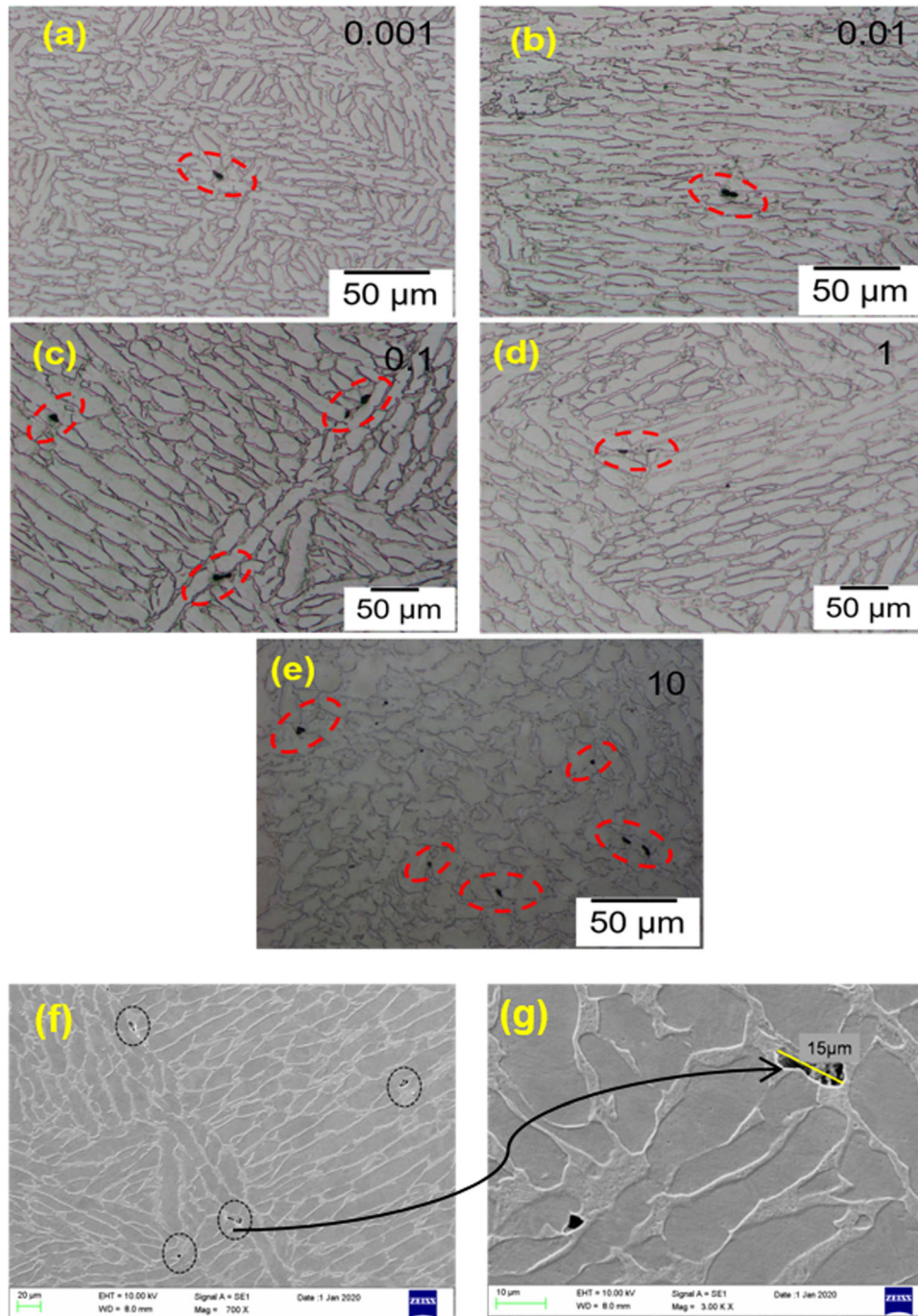


Fig.7 (a-e) Optical microstructure of hot-compressed specimen of 800 °C at strain rates of 0.001, 0.01, 0.1, 1 and 10 s^{-1} showing strain-induced porosities, (f-g) SEM image of hot-compressed specimen at 800 °C, 1 s^{-1} showing strain-induced porosities along the grain boundaries

tions varies with the nature of cooling and holding time also. As per the investigations of Lin et al., globularization behavior of the lamellar phase was observed at 950-960 °C when the alloy underwent air cooling/furnace cooling (Ref 23).

During isothermal compression, recrystallized microstructures were found in the material in the temperature range of 800-900 °C. Dynamic recovery and recrystallization mechanisms act as the driving force for the formation of recrystallized grains during hot deformation. Dynamic recrystallization in the $\alpha - \beta$ range occurs by shearing of α platelets and globularization of lamellar structure. Dislocation movement also plays an important role in the recrystallization to globular structure (Ref 22, 24).

3.4 Kinetics Analysis

The relationship between peak stress and $\ln(\dot{\epsilon})$ at different temperatures was determined as depicted in Fig. 9(a) and (b). The relationship between $1000/T$ and $\ln[\sinh(\alpha\sigma)]$ at different strain rates, the relationship between $\ln[\sinh(\alpha\sigma)]$ and $\ln(\dot{\epsilon})$ and the relationship of $\ln[\sinh(\alpha\sigma)]$ versus $\ln Z$ at different temperatures are presented in Fig. 10(a), (b) and (c). Constitutive equations based on Arrhenius models have been used to predict the flow behavior of Ti6Al4V material and thereby optimizations of parameters like temperature, strain rate and stress during thermomechanical processing. Power law, exponential

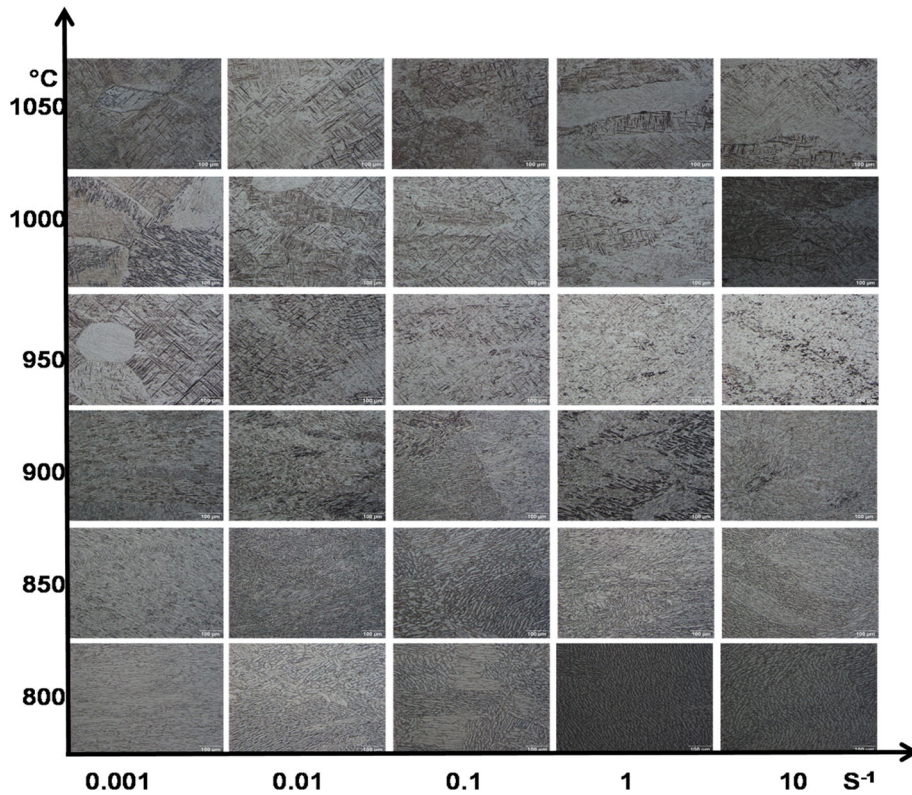


Fig. 8 Microstructural mapping of hot isostatically compressed specimens at different temperatures and strain rates

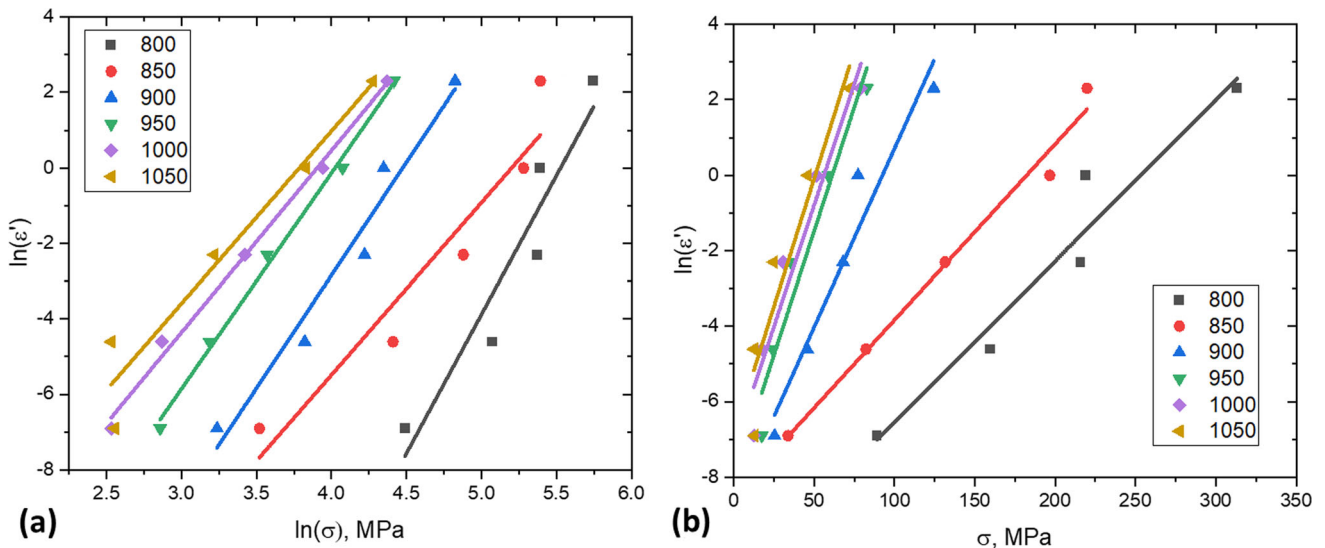


Fig. 9 (a) Relationship between peak stress and $\ln(\dot{\epsilon})$ at different temperatures (b) Relationship between $\ln(\text{peak stress})$ and $\ln(\dot{\epsilon})$ at different temperatures

law and hyperbolic law are referred (Ref 24) and Zener–Hollomon parameters (Z) are used to define the temperature-compensated strain rate at various temperature and stress levels as given in Eq 1.

$$Z = \dot{\epsilon} \exp\left(\frac{Q}{RT}\right) = \begin{cases} A_1 \sigma^{n_1}, & \alpha \sigma < 0.8 \\ A_2 \exp \beta \sigma, & \alpha \sigma < 1.2 \\ A [\sinh(\alpha \sigma)]^n, & \alpha \sigma \text{ for all} \end{cases} \quad (\text{Eq 1})$$

In the equation, power law is used to describe the strain rate at low stress levels ($\alpha \sigma < 0.8$) and exponential law is used to describe high stress levels ($\alpha \sigma < 1.2$). Hyperbolic law is used to express the temperature-compensated strain rate for the entire range of stress. The value of constants (A_1 , A_2 , n_1 , n , α , β) and Z , Q is obtained using various equations presented elsewhere (Ref 24).

The activation energy was calculated for all hot deformation temperatures which are presented in Fig. 11. The lowest

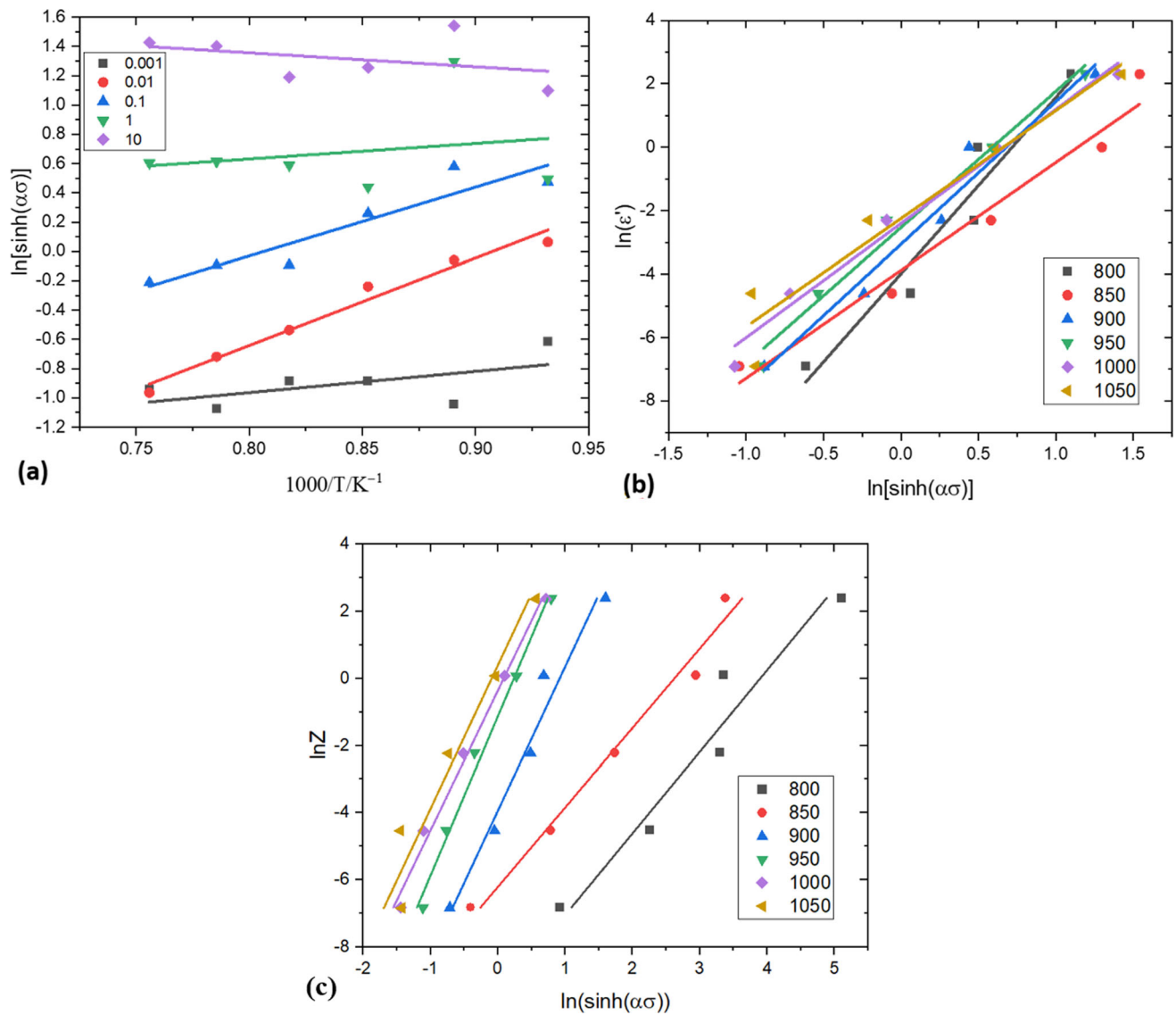


Fig. 10 (a) Relationship between $1000/T$ and $\ln[\sinh(\alpha\sigma)]$ at different strain rates, (b) Relationship between $\ln[\sinh(\alpha\sigma)]$ and $\ln(\dot{\epsilon})$ at different temperatures, (c) Relationship between $\ln[\sinh(\alpha\sigma)]$ and $\ln Z$ at different temperatures

activation energy was observed at 800 °C and it is showing a trend of increasing as temperature increases and reaches a maximum at 950 °C and then decreases thereafter with the rise of temperature. The activation energy was obtained as an average of 620.62 kJ/mol for the temperature range 750-950 °C. The difficulty in the deformation process is interpreted based on this activation energy. Since the α - β transition temperature of Ti6Al4V material is 980 °C, the volume fraction of α phase will be more than that of β phase below this temperature and the fraction of β phase increases as the temperature exceeds β transus temperature. This contributes toward the variation in activation energy with an increase in deformation temperature. At lower temperature range < 900 °C, both DRX and DRV coexist, but DRX dominates over DRV and at high temperatures > 900 °C, DRX is the main softening mechanism. At higher temperatures > 980 °C, the material transforms to β phase and the deformation happens in β regime.

3.5 Processing Map

Dynamic materials modeling (DMM) is a well-established modeling technique for explaining the flow behavior of the material at different hot deformation conditions. Efficiency of power dissipation and strain rate sensitivity are the two prime parameters in DMM. The processing maps obtained at different strains 0.1, 0.2, 0.3 and 0.4 representing the material response to the hot deformation conditions were generated with temperature versus $\log(\text{strain rate})$ ($\dot{\epsilon}$). The efficiency of power dissipation was calculated as a function of temperature and strain rate and plotted as power efficiency contour maps. Contour maps of the efficiency of power dissipation (η), strain rate sensitivity parameter (m) and instability map at different strain values, $\epsilon = 0.1, 0.2, 0.3, 0.4$ and 0.5 , are obtained and representative at 0.2 and 0.4 strain is presented in Fig. 12(a), (b), (c), (d), (e) and (f).

The efficiency of power dissipation map represents the power dissipated through various metallurgical processes like dynamic recovery, dynamic recrystallization, plastic flow and

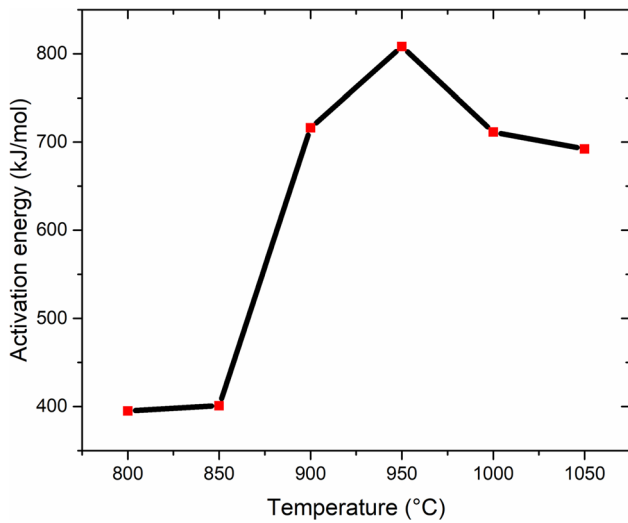


Fig. 11 Graph showing the variation of activation energy verses hot deformation temperatures

formation of metallurgical defects. The peaks of m and η signify deformation mechanisms. A higher η value shows favorable stable region during hot working which indicates that a larger proportion of power is consumed for the microstructural evolution. The stable and unstable regions are identified in the instability map.

Along with the microstructural changes occurring in the material during hot compression, some energy is consumed for the formation of defects also in the material. So, only efficiency maps are not enough for the calculation of favorable and stable regions of working and hence instability criteria are also considered for interpreting the stable regions. Detailed equations on power dissipation are given elsewhere (Ref 25). Following the dynamic material model, the condition for the metallurgical instability is predicted by continuum instability criterion Ref (Ref 22) given by

$$\zeta(\dot{\epsilon}) = \frac{mP}{J} - 1 = \frac{2m}{\eta} - 1 < 0 \quad (\text{Eq 2})$$

where P is energy per unit volume, J is co-dissipation of energy, m is strain rate sensitivity parameter, and η is the efficiency of power dissipation.

The instability maps were developed using the continuum instability criterion ζ . The material flow instabilities are predicted to occur when the continuum instability criterion ζ is negative.

Considering the strain value, $\epsilon = 0.2$, the stable regions are bifurcated into two domains, domain I corresponds to 825-850 °C at strain rates of 10^0 to 10^{-3} s^{-1} and domain II is in the range of 850-1025 °C and strain rate 10^{-3} to 10^{-2} s^{-1} avoiding a small unstable region at 950-1000 °C and strain rate $10^{0.5}$ to 10^1 s^{-1} since α to β transition occurs in Ti6Al4V in that temperature range. At strain 0.4, the stable regions were found in the almost same range of temperature and strain rate, i.e., 825-875 °C at strain rates of 10^0 to 10^{-3} s^{-1} , 875-925 °C at strain rates of 10^{-3} to $10^{-1.5} \text{ s}^{-1}$ and 925-1000 °C at strain rates of 10^{-3} to $10^{0.5} \text{ s}^{-1}$.

Along with processing maps, the efficiency of power dissipation map also needs to be considered to find the correct stable region of hot working. As per the efficiency of power

dissipation maps, the maximum efficiency of 65-70 % is obtained in the temperature range of 825-900 °C and strain rate 10^{-3} to $10^{-2.5} \text{ s}^{-1}$ at all the strain values 0.1, 0.2, 0.3 and 0.4. The higher value of efficiency means more power dissipated through dynamic recrystallization which indicated a stable flow of material without any defects.

3.6 Comparison of Constitutive Modeling Equations and Prediction Capability

The flow stress behavior and its dependence on stress, temperature and strain rate and other metallurgical parameters are interpreted using constitutive modeling equations. Along with dynamic recovery (DRV) and recrystallization (DRX) mechanisms, unstable material flow also occurs along with the formation of defects and unfavorable microstructure. Optimization of processing parameters is essential to avoid the formation of these kinds of inhomogeneity conditions. Different constitutive models, like Johnson-Cook (JC) model, modified Johnson-Cook (m-JC) model and artificial neural network (ANN), were implemented to formulate the constitutive relationship to simulate the hot deformation behavior of Ti6Al4V in the specified range of temperature and strain rate (Ref 26-30).

JC model and m-JC model are phenomenological models where empirical relationships using mathematical functions are used to predict the flow behavior. It requires only less material constants and less computation time, which makes them more convenient for simulation. However, these models are unable to provide complete information about the hot deformation and only experimental data fitting is possible. Arrhenius equation model is a physically based model which can provide more accurate information about physical aspects of hot deformation compared to phenomenological models. However, this model involves more material constants and requires a wide range of experimental data. The material constants in the constitutive equations are evaluated through the fitting of curves and regression. Since hot deformation is a highly complex and nonlinear phenomenon over a wide range of temperatures and strain rates, the accurate prediction of flow stress behavior is difficult by JC, m-JC and Arrhenius equation models. However, the ANN model is capable of predicting the behavior of complex systems like hot deformation, and hence, it is considered the best-preferred approach for simulating the nonlinear flow stress data.

3.6.1 Arrhenius Model. Arrhenius equations are used to model the flow stress behavior. Based on Arrhenius equations Eq 1 can be modified as,

$$\dot{\epsilon} = A[\sinh(\alpha\sigma)]^n e^{-\frac{Q}{RT}} \quad (\text{Eq 3})$$

The equation can be further modified to obtain the flow stress as,

$$\sigma = \frac{1}{\alpha} \ln \left[\left[\frac{Z}{A} \right]^{\frac{1}{n}} + \left\{ \left[\frac{Z}{A} \right]^{\frac{2}{n}} + 1 \right\}^{\frac{1}{2}} \right] \quad (\text{Eq 4})$$

Values of the Z , A , α and n obtained previously were substituted to predict flow stress behavior for each temperature and strain rate. The coefficients calculated as per Arrhenius model are $a = 0.018514$ & $n = 3.5974833$. Comparison of experimental and calculated flow stress as per the Arrhenius model is represented in Fig. 13(a).

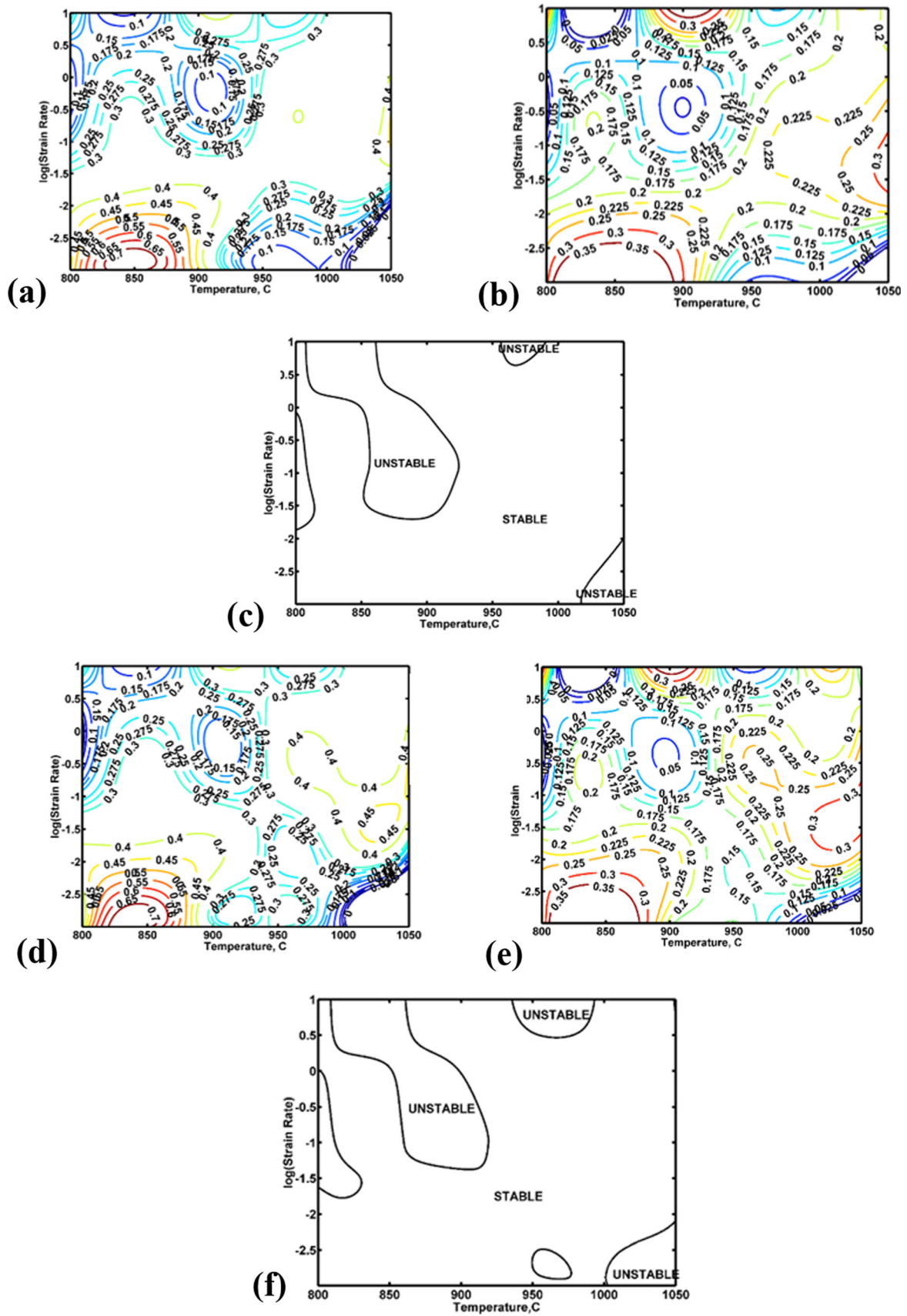


Fig. 12 Processing maps, (a) efficiency of power dissipation, η (b) strain rate sensitivity, m (c) and instability map at a strain of 0.2, (d) efficiency of power dissipation, η (e) strain rate sensitivity, m (f) and instability map at a strain of 0.4

3.6.2 Modified Johnson–Cook (m-JC) Model. According to JC model, only strain hardening, strain rate hardening and thermal softening were considered as independent phenomena and the combined effect of strain, strain rate and temperature was not considered. Hence, the JC model was modified by Zhang et al. (Ref 10), Hou and Wang and Lin et al. (Ref 29-31) to improve the quality and accuracy of simulation by considering all these parameters. m-JC model formulates the flow stress as follows:

$$\sigma = (A_1 + B_1\varepsilon + B_2\varepsilon^2)(1 + C_1 \ln \dot{\varepsilon}^*) \cdot \exp[(\lambda_1 + \lambda_2 \ln \dot{\varepsilon}^*)(T - T_r)] \quad (\text{Eq 5})$$

$$\ln \left\{ \frac{\sigma}{(A + B\varepsilon + C\varepsilon^2)(1 + C_0 \ln \dot{\varepsilon}^*)} \right\} = [(\lambda_1 + \lambda_2 \ln \dot{\varepsilon}^*)(T - T_r)] \quad (\text{Eq 6})$$

where $A, B, C, C_0, \lambda_1, \lambda_2$ are materials constants and the other parameters are similar to that of JC model.

The flow stress is compared with the experimental data and predicted the behavior of flow stress and the calculated values

of the coefficients A, B, C and C_0 are obtained as 154, 139.4, – 400.7 and 0.1571, respectively.

At the reference temperature and strain rate, Eq 5 reduced to

$$\frac{\sigma}{(A + B\varepsilon + C\varepsilon^2)} = (1 + C_0 \ln \dot{\varepsilon}^*) \quad (\text{Eq 7})$$

A graph is plotted between $\frac{\sigma}{(A+B\varepsilon+C\varepsilon^2)}$ and $(\ln \dot{\varepsilon}^*)$, linear fitting is carried out, and C_0 is obtained from the slope of the linear fit (Fig. 13b).

The values of $\lambda_1 + \lambda_2 \ln \dot{\varepsilon}^*$ obtained by linear fitting of $\ln \left\{ \frac{\sigma}{(A+B\varepsilon+C\varepsilon^2)(1+C_0 \ln \dot{\varepsilon}^*)} \right\}$ vs $(T - T_r)$ at strain rate of 0.1, 1 and 10 of $\lambda_1 + \lambda_2 \ln \dot{\varepsilon}^*$ values were plotted against $\dot{\varepsilon}$ to obtain λ_1 and λ_2 . The values of λ_1 and λ_2 obtained from the linear fitting of $(\lambda_1 + \lambda_2 \ln \dot{\varepsilon}^*)$ vs. $\ln \dot{\varepsilon}^*$ plot as – 0.00736 and 5.65×10^{-4} .

3.6.3 Artificial Neural Network (ANN). ANN is a mathematical modeling in which the input is transformed into output by mathematical operations in a series of layers. Three layers—input layer, hidden and output layers—are used for a typical ANN. The data in each layer are transformed by

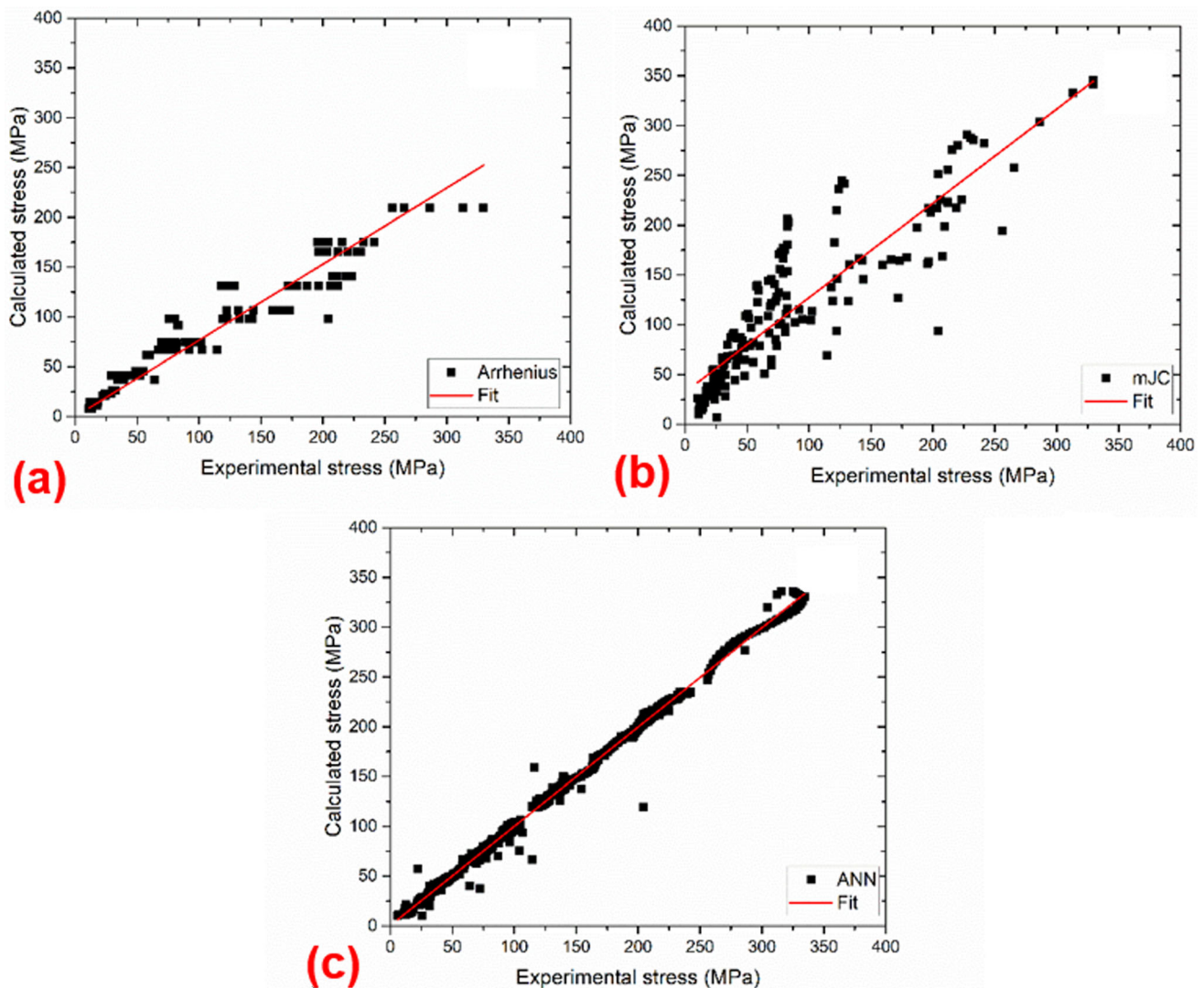


Fig. 13 Plots showing the relationship between the experimental and calculated flow stress: (a) Arrhenius model, (b) Modified Johnson–Cook model and (c) Artificial neural network

activation functions and incorporation of weights and biases and transferred to the next layer. The input layer consists of variables like strain, strain rate and temperature and the flow stress will be the output variable. The preprocessed data are fed to the neural network system and both the input and output variables are normalized to achieve efficient output using the relationship provided below.

$$P_n = 0.1 + 0.8 \frac{(P - P_{\min})}{(P_{\max} - P_{\min})} \quad (\text{Eq 8})$$

where P_n is the normalized value of parameter P , P_{\max} and P_{\min} are the maximum and minimum values of P , respectively. Since the strain rate parameter is very small for processing using ANN, different equation has been developed for that purpose as shown below

$$\dot{\epsilon}_n = 0.1 + 0.8 \frac{\log \dot{\epsilon} - \log \dot{\epsilon}_{\min}}{\log \dot{\epsilon}_{\max} - \log \dot{\epsilon}_{\min}} \quad (\text{Eq 9})$$

Hyperparameters, such as number of hidden layer neurons, activation functions and training algorithms, were evaluated before finalizing the ANN model. Bayesian regularization, Levenberg–Marquardt and standard conjugate method were considered as training algorithms. Logistic sigmoid, tansigmoid and pure linear were considered for activation functions. Absolute average error (AARE) was used for evaluating the ANN model. A number of neurons in hidden layers were chosen based on iteratively changing and comparing the AARE. Bayesian regularization as the training algorithm and tansigmoid as the transfer function were found to be giving the best AARE. The stress–strain data were split into three sets for training, validation and testing in the ratio 70:15:15. The number of neurons in the hidden layer is chosen as 10.

Comparison of experimental and calculated flow stress for all the models is represented in Fig. 13(a), (b) and (c).

A statistical parameter called correlation coefficient (R) and average absolute relative error (AARE) were defined to predict and quantify the accuracy of the constitutive equations R and AARE values were calculated as per the equations given below (Ref 32).

$$R = \frac{\sum_{i=1}^N (E_i - \bar{E})(P_i - \bar{P})}{\sqrt{\sum_{i=1}^N (E_i - \bar{E})^2 \sum_{i=1}^N (P_i - \bar{P})^2}} \quad (\text{Eq 10})$$

$$\text{AARE} = \frac{1}{N} \sum_{i=1}^N \left| \frac{E_i - P_i}{E_i} \right| \quad (\text{Eq 11})$$

where E_i is the experimental data and P_i is the predicted value. \bar{E} and \bar{P} are the mean values of E and P , respectively. N is the total number of data sets used.

R and AARE values were obtained for all the models—Arrhenius model, m-JC model and artificial neural network as provided in Table 3. Among all these models, ANN model gives the best fit with AARE 0.0417 and R value 0.9985.

3.7 Hot Rolling Studies of Ti6Al4V

The microstructure of Ti6Al4V material hot rolled at different temperatures of 800, 850, 900 and 950 °C is presented in Fig. 14. Figure 14(a) shows the optical microstructure Ti6Al4V disk after hot rolling at 800 °C which shows that the

Table 3 R and AARE values of constitutive models

Model	R	AARE
Arrhenius	0.9821	0.7694
m-JC	0.9560	0.6363
ANN	0.9985	0.0417

coarse acicular $\alpha + \beta$ Widmanstätten microstructure has elongated with rolling temperature. It means that significant dynamic recrystallization did not occur during the hot rolling at 800 °C since the rolling temperature is much below the beta transus temperature. The microstructure appeared non-uniform with kinking of alpha at some places. Comparing the microstructure of hot-rolled Ti6Al4V disk at 850 °C with hot rolling at 900 °C revealed elongated microstructure, but the percentage of elongation was slightly reduced. The kinking or wavy nature is also reduced on rolling to the higher temperature of 900 °C. Along with the elongated alpha grains, a few fine alpha grains are also visible in the microstructure which indicates that the dynamic recrystallization process has started at this temperature and a few grains were recrystallized. The microstructure of the hot-rolled Ti6Al4V disk at 950 °C revealed a phase transformation from lamellar structure to equiaxed microstructure due to dynamic recrystallization. At 950 °C, the microstructure revealed a bimodal $\alpha + \beta$ microstructure. Figure 15(a) shows the optical microstructure revealing the presence of strain-induced porosity and Fig. 15(b) shows the formation of cracks at the edges of the hot-rolled specimen at 800°C. SEM image as shown in Fig. 15(c) and (d) shows the strain-induced porosity in the microstructure at higher magnification. The materials did not reveal the formation of any of the defects like cracks or strain-induced porosities at the test conditions 850, 900 and 950 °C. It indicates that SIP is not forming at high temperatures > 850 °C.

To investigate the effect of rolling temperature on mechanical properties, tensile testing of hot-rolled specimens was carried out and Fig. 16(a) represents stress–strain curve of the specimens after hot rolling at different temperatures. The specimens rolled between 850 and 950 °C show marginal difference in flow stress. Luo Yumeng et al. extensively studied the effect of rolling on the mechanical properties of Ti6Al4V and found that an anisotropy in mechanical properties exists with rolling direction and the material loaded along the rolling direction exhibited the best ductility and the material loaded in the normal to rolling direction shown maximum flow stress (Ref 33). The fracture surface analysis by SEM revealed dimple features typical of ductile mode of failure in all the samples (Fig. 17a-d). The fractography observation on the hot-rolled specimen at 800°C as shown in Fig. 17(a) also confirms the presence of strain-induced porosity. The dimples are less deep in the case of specimen hot rolled at 850 °C (Fig. 17b) indicates less plasticity and high-temperature rolled specimens revealed deep equiaxed dimples which revealed better plasticity and the same trend is seen in flow stress curves also. This clearly indicates as the temperature decreases flow stress increases and the possibility of strain-induced porosity generation increases at a further lower temperature as observed through hot compression test.

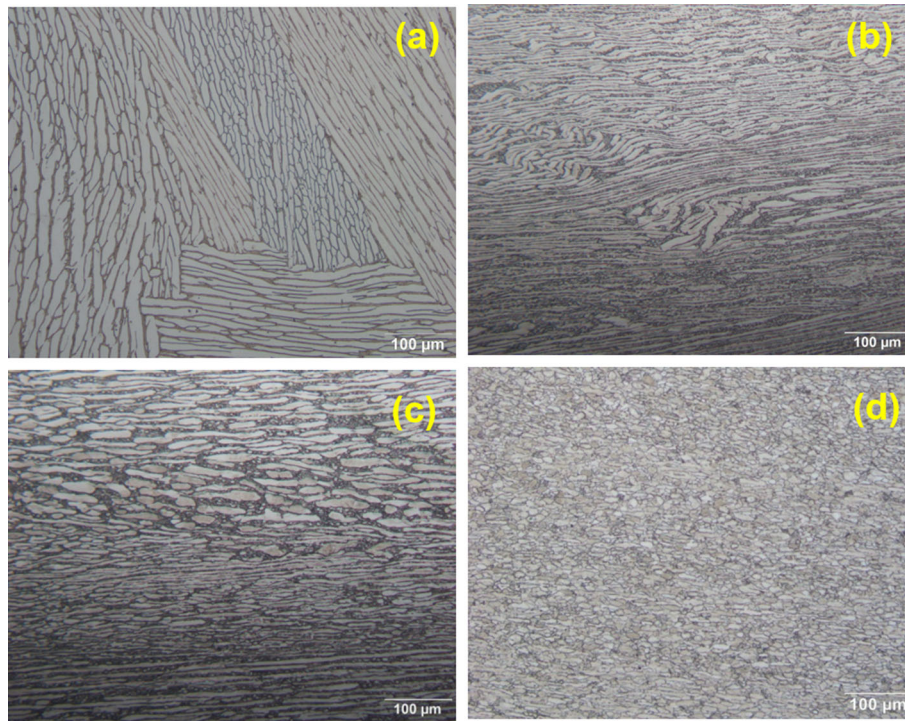


Fig. 14 Optical microstructures of hot-rolled samples at different temperatures—(a) hot rolled @ 800 °C, (b) hot rolled @ 850 °C, (c) hot rolled @ 900 °C, (d) hot rolled @ 950 °C

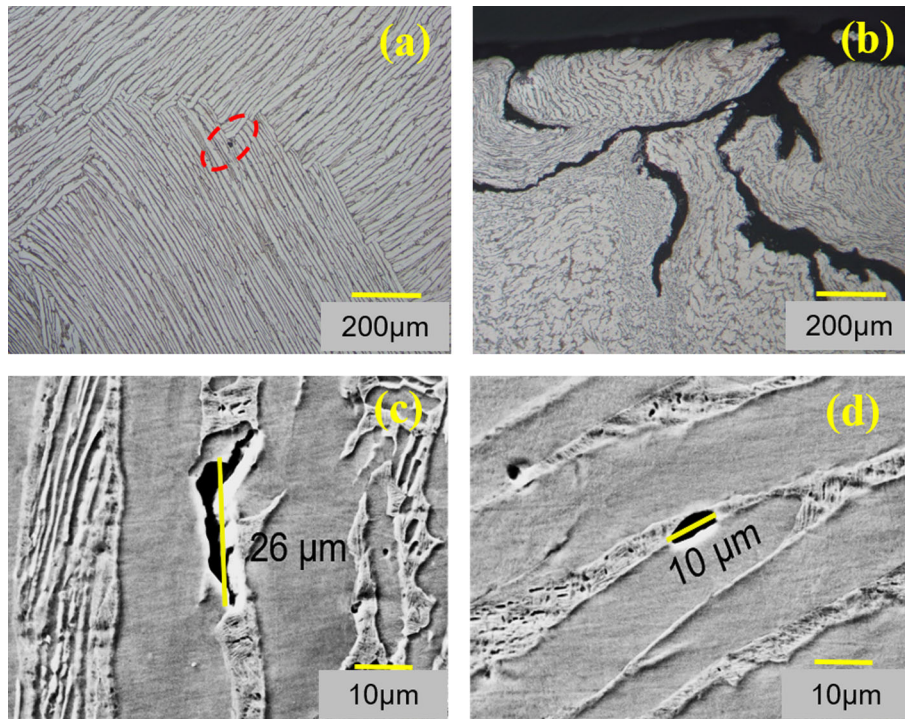


Fig. 15 (a) Optical microstructure of hot-rolled samples at 800 °C showing strain-induced porosity, (b) Optical microstructure of hot-rolled samples at 800 °C showing cracks at the edges of the rolled specimen, (c & d) SEM images of hot-rolled samples at @ 800 °C showing strain-induced porosities at different locations

3.8 EBSD Analysis of Isothermally Hot-Compressed Specimens

In order to extensively investigate the microstructural transformation of the alloy with temperature, the hot-compressed specimens at 800, 850, 950 and 1000 °C and strain rate 0.1 s^{-1} have been analyzed using EBSD. Figure 18 shows EBSD analysis band contrast (BC) + Inverse pole Figure (IPF) + Grain boundary (GB) distribution of hot-compressed samples. As temperature increases, the phase morphology changes marginally from 800 to 850 °C then at

950 °C transformation to β phase is observed and after crossing the transition temperature ($\sim 980 \text{ °C}$), the microstructure fully transformed to needle shaped β phase. At the temperatures 800 and 850 °C, the microstructure predominantly contains the low-angle grain boundaries (misorientation $< 10^0$). But at higher temperatures 950 and 1000 °C, an inverse scenario is noticed that the proportion of high-angle grain boundaries (misorientation $> 10^0$) increases with temperature. It is in line with the observation noted in optical microscopy showing Widmanstatten-type structure (Fig. 8) at high-temperature deformation. Transformation to β phase is clearly indicated in EBSD results showing the presence of β phases at grain boundaries of α phases at 800 °C deformed samples with high volume fraction of low-angle boundaries. As the temperature increases, these dynamically recrystallized grains grow and so the volume fraction of high-angle boundaries ($> 10^0$) increases indicating transformation of α to β . This indicates that high-angle grain boundaries promote β phase transformation (Ref 33, 34). At 950 °C and above, volume fraction of β phases are higher with Widmanstatten-type structure. The corresponding EDS elemental mapping is provided in Fig. 19 indicating transformation of β phase with increase in temperature.

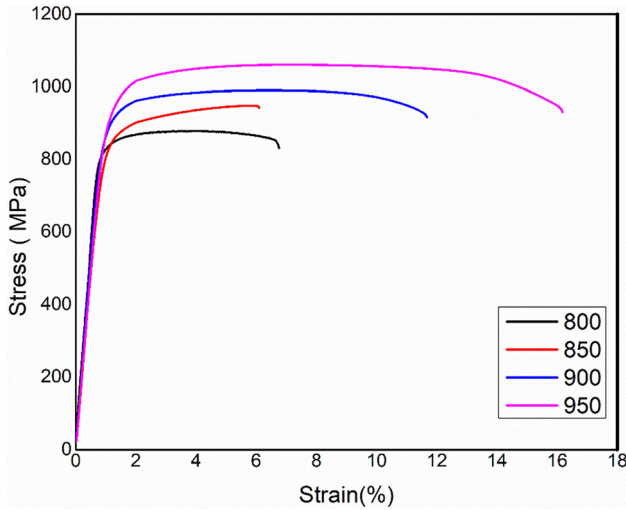


Fig. 16 Engineering stress–strain curve of tensile tested Ti6Al4V hot rolled at different temperatures (legends shown in Fig. is in °C)

4. Conclusions

Based on the detailed hot workability study conducted on Ti6Al4V in the temperature range of 800-1050 °C and strain rate of $0.001\text{-}10 \text{ s}^{-1}$ followed by processing maps and kinetics analysis, the conclusions are listed as follows.

- Stress–strain curves exhibited flow softening or steady-state flow indicative of dynamic recrystallization. Homo-

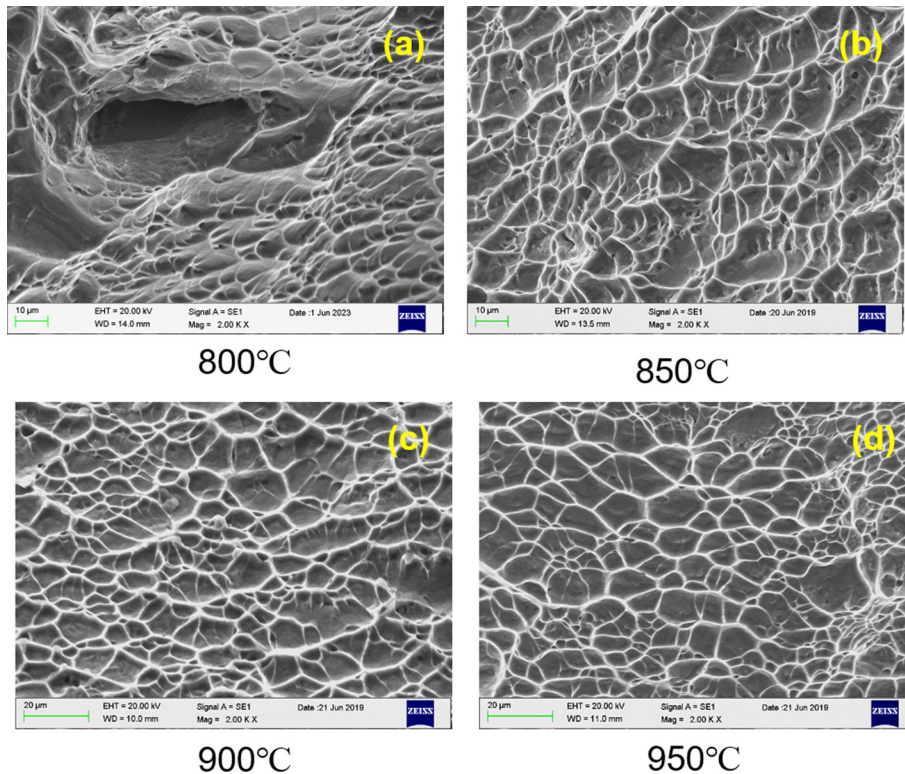


Fig. 17 SEM fractography images of tensile tested Ti6Al4V hot rolled at different temperatures

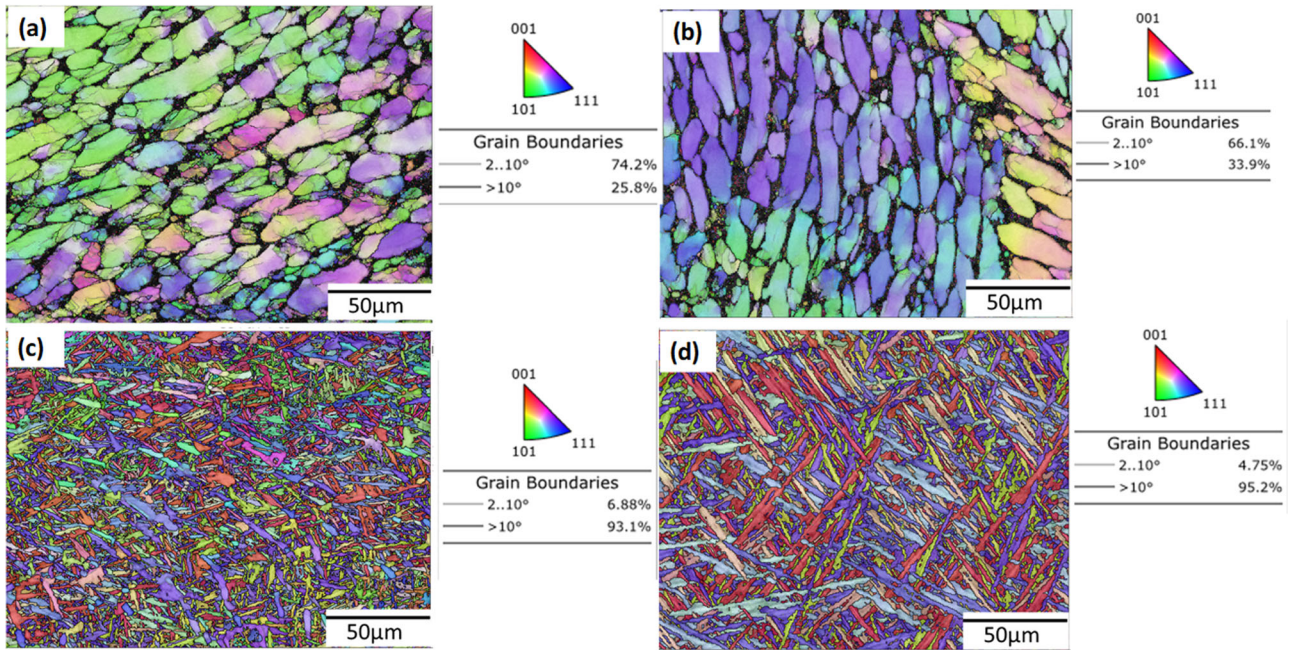


Fig. 18 EBSD analysis BC + IPF + GB distribution of hot-compressed samples, a) at 800 °C and strain rate 0.1 s⁻¹, b) 850 °C and strain rate 0.1 s⁻¹, c) 950 °C and strain rate 0.1 s⁻¹ and d) 1000°C and strain rate 0.1 s⁻¹

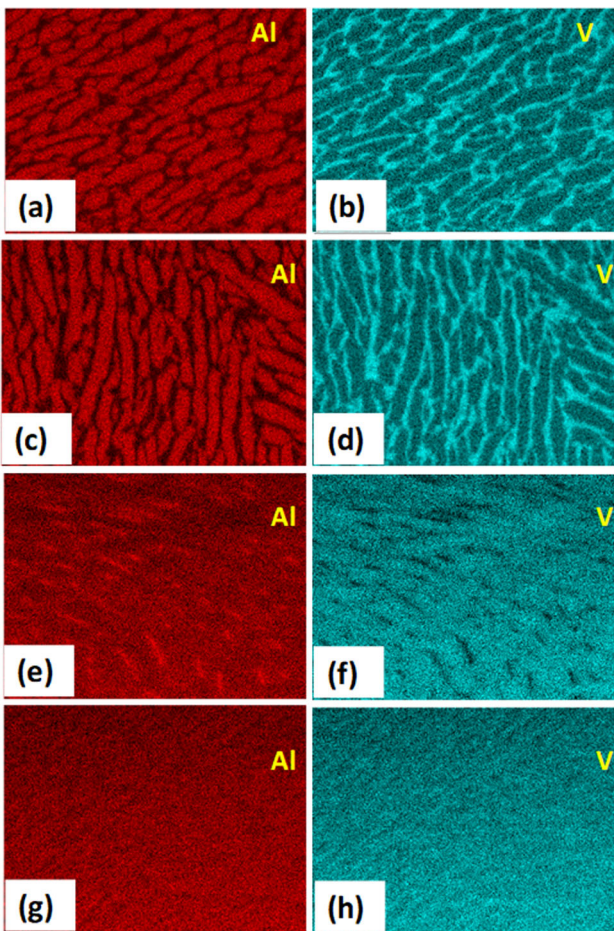


Fig. 19 EDS analysis in hot-compressed samples (a & b) 800 °C and strain rate 0.1 s⁻¹, (c & d) 850 °C and strain rate 0.1 s⁻¹, (e & f) 950 °C and strain rate 0.1 s⁻¹ and (g & h) 1000 °C and strain rate 0.1 s⁻¹

geneous material flow was observed without the presence of any defects under all test conditions above 850 °C. Strain-induced porosities were observed in the hot-compressed samples deformed at 800 °C at all strain rates. The Ti6Al4V specimen hot rolled at 800 °C also confirmed the presence of strain-induced porosities.

- The flow stress is found to have an increasing trend with increase in strain rate and decrease in temperature.
- The activation energy was calculated for all hot deformation temperatures which has shown a trend of increase as temperature increases and reaches maximum at 950 °C and then decreases.
- As per the efficiency of power dissipation maps, the maximum efficiency of 65-70 % is obtained in the temperature range of 825-900 °C and strain rate 10⁻³ to 10^{-2.5} s⁻¹ at all the strain values 0.1, 0.2, 0.3 and 0.4.
- At the temperatures 800°C and 850°C, the microstructure predominantly contains the low-angle grain boundaries, but the proportion of high-angle grain boundaries increases with temperature which promotes β phase transformation. At the temperatures \geq 950 °C, volume fraction of β phases is higher with Widmanstatten-type structure.
- The deformation behavior was interpreted based on the constitutive equation models like the modified Johnson-Cook (m-JC) model and artificial neural network (ANN) and the accuracy of models—Arrhenius model, m-JC model and artificial neural network were quantified. Among all these models, ANN model gives the best fit with AARE 0.0417 and *R* value 0.9985.

Acknowledgments

Authors wish to express their deep sense of gratitude to Group Director, Materials and Metallurgy Group and Deputy Director,

Materials and Mechanical Entity for their encouragement and support during this work. Authors are thankful to Aerospace materials lab team, LPSC, for the support provided for the isothermal compression test carried out in Gleeble thermomechanical simulator.

References

1. M. Peters and C. Leyens, Aerospace and Space Materials, Materials Science and Engineering – vol. III
2. E.B. Shell and S.L. Semiatin, Effect of Initial Microstructure on Plastic Flow and Dynamic Globularization during Hot Working of Ti-6Al-4V, *Metall. Mater. Trans. A*, 1999, **30**, p 3219–3229.
3. Z.X. Zhang, S.J. Qu, A.H. Feng, and J. Shen, Achieving Grain Refinement and Enhanced Mechanical Properties in Ti-6Al-4V Alloy Produced by Multidirectional Isothermal Forging, *Mater. Sci. Eng. A*, 2017, **692**, p 127–138.
4. S.L. Semiatin, V. Seetharaman, and I. Weiss, The Thermomechanical Processing of alpha/beta Titanium Alloys, *J. Mater. Sci.*, 1997, **49**, p 33–39.
5. C. Leyens and M. Peters, *The metallurgy of titanium alloys Titanium and Titanium Alloys: Fundamentals and Applications*, Wiley-VCH GmbH Germany, Germany, 2003, p 4–5
6. M. Peters, A. Gysler, G. Liitjering, Titanium 80, 4th International Conference on Titanium, Kyoto, Japan, 1980, pp. 1777–86
7. T. Seshacharyulu, S.C. Medeiros, W.G. Frazier, and Y.V.R.K. Prasad, Microstructural Mechanisms during Hot Working of Commercial Grade Ti-6Al-4V with Lamellar Starting Structure, *Mater. Sci. Eng. A*, 2002, **325**, p 112–125.
8. J. Cai, K. Wang, P. Zhai, F. Li, and J. Yang, A Modified Johnson-Cook Constitutive Equation to Predict Hot Deformation Behavior of Ti-6Al-4V Alloy, *J. Mater. Eng. Perform.*, 2015, **24**, p 32–44. <https://doi.org/10.1007/s11665-014-1243-x>
9. T. Sheppard and J. Norley, Deformation Characteristics of Ti-6Al-4V, *Mater. Sci. Technol.*, 1988, **4**, p 903–908.
10. W. Zhang, H. Ding, J. Zhao, B. Yang, W. Yang, and I. Introduction, Hot Deformation Behavior and Processing Maps of Ti-6Al-4V Alloy with Starting Fully Lamellar Structure, *J. Mater. Res.*, 2018 <https://doi.org/10.1557/jmr.2018.331>
11. P.M. Souza, H. Beladi, B. Rolfe, R. Singh, and P.D. Hodgson, Softening Behavior of Ti6Al4V Alloy During Hot Deformation, *Mater. Sci. Form*, 2015, **829**, p 407–412. <https://doi.org/10.4028/www.scientific.net/MSF.828-829.407>
12. P.M. Souza, J. Mendiguren, Q. Chao, H. Beladi, P.D. Hodgson, and B. Rolfe, A Microstructural Based Constitutive Approach for simulating Hot Deformation of Ti6Al4V Alloy in the $\alpha + \beta$ Phase Region, *Mater. Sci. Eng. A*, 2019, **748**, p 30–37. <https://doi.org/10.1016/j.msea.2019.01.081>
13. Y.C. Lin, C.Y. Zhao, M.S. Chen, and D.D. Chen, A Novel Constitutive Model for Hot Deformation Behaviors of Ti-6Al-4V Alloy Based on Probabilistic Method, *Appl. Phys. A*, 2016, **122**, p 71.
14. Y.C. Lin, Q. Wu, G.D. Pang, X.Y. Jiang, and D.G. He, Hot Tensile Deformation Mechanism and Dynamic Softening Behavior of Ti-6Al-4V Alloy with Thick Lamellar Microstructures, *Adv. Eng. Mater.*, 2020, **22**, p 1901193.
15. N. Nayan, R.K. Gupta, V. AnilKumar, Y. Maruti Prasad, and S.V.S.N. Murty, Metallurgical Investigation and Root Cause Analysis of Defects in a Ti Alloy (Ti6Al4V) Propellant Tank Ring, *J. Preven. Fail. Anal.*, 2023 <https://doi.org/10.1007/s11668-023-01712-w>
16. M.M. Uz, A.B. Hazar Yoruç, O. Cokgunlu, C.S. Aydoğan, and G.G. Yapici, A Comparative Study on Phenomenological and Artificial Neural Network Models for High Temperature Flow Behavior Prediction in Ti6Al4V Alloy, *Mater. Today Commun.*, 2022, **33**, p 104933. <https://doi.org/10.1016/j.mtcomm.2022.104933>
17. H. Ming, L. Dong, Z. Zhang, X. Lei, R. Yang, and Y. Sha, Correction of Flow Curves and Constitutive Modelling of a Ti-6Al-4V Alloy, *Metals*, 2018, **8**, p 256. <https://doi.org/10.3390/met8040256>
18. I. Weiss, R. Srinivasan, P.J. Bania, D. Eylon, and S.L. Semiatin, *Advances in the Science and Technology of Titanium Alloy Processing*, TMS, Warrendale, Pennsylvania, 1996, p 349–367
19. E.W. Collings, G. Welsch, and R. Boyer, *Materials Properties Handbook: Titanium Alloys*, ASM International, Detroit, 1994
20. T. Seshacharyulu, S.C. Medeiros, W.G. Frazier, and Y.V.R.K. Prasad, Hot Working of Commercial Ti-6Al-4V with an Equiaxed a-b Microstructure: Materials Modeling Considerations, *Mater. Sci. Eng. A*, 2000, **284**, p 184–194.
21. H. Margolin and P. Cohen, Titanium '80, 4th International Conference on Titanium, Kyoto, Japan, 1980, pp. 1555–61
22. Y.V.R.K. Prasad and S. Sasidhara Eds., *Hot Working Guide: A Compendium of Processing Maps*, ASM International, Materials Park, OH, 1997
23. Y.C. Lin, X.Y. Jianga, C.J. Shuaib, C.Y. Zhaoa, D.G. Hea, M.S. Chenb, and C. Chend, Effects of Initial Microstructures on Hot Tensile Deformation Behaviors and Fracture Characteristics of Ti-6Al-4V Alloy, *Mater. Sci. Eng. A*, 2018, **711**, p 293–330.
24. S.L. Semiatin, R.L. Goetz, E.B. Shell, V. Seetharaman, and A.K. Ghosh, Cavitation and Failure during Hot Forging of Ti-6Al-4V, *Metall. Mater. Trans. A*, 1999, **30A**, p 1411–1424.
25. R.K. Gupta, S.V.S. Narayana Murty, B. Pant, V. Agarwala, and P.P. Sinha, Hot Workability of $\gamma+\alpha 2$ Titanium Aluminide: Development of Processing Map and Constitutive Equations, *Mater. Sci. Eng. A*, 2012, **551**, p 169–186.
26. M. Hu, L. Dong, Z. Zhang, X. Lei, R. Yang, and Y. Sha, Correction of Flow Curves and Constitutive Modelling of a Ti-6Al-4V Alloy, *Metals*, 2018, **8**, p 1–15. <https://doi.org/10.3390/met8040256>
27. G.R. Johnson, A Constitutive Model and Data for Materials Subjected to Large Strains, High Strain Rates, and High Temperatures, *Proc. 7th Int. Sympo. Ballist.* (1983) 541–547
28. H. Zhang, W. Wen, and H. Cui, Behaviors of IC10 Alloy Over a Wide Range of Strain Rates and Temperatures: Experiments and Modeling, *Mater. Sci. Eng. A*, 2009, **504**, p 99–103. <https://doi.org/10.1016/j.msea.2008.10.056>
29. Q.Y. Hou and J.T. Wang, A Modified Johnson-Cook Constitutive Model for Mg-Gd-Y Alloy Extended to a Wide Range of Temperatures, *Comput. Mater. Sci.*, 2010, **50**, p 147–152. <https://doi.org/10.1016/j.commatsci.2010.07.018>
30. Y.C. Lin, X.M. Chen, and G. Liu, A Modified Johnson-Cook Model for Tensile Behaviors of Typical High-strength Alloy Steel, *Mater. Sci. Eng. A*, 2010, **527**, p 6980–6986. <https://doi.org/10.1016/j.msea.2010.07.061>
31. D. Samantaray, S. Mandal, A.K. Bhaduri, and P.V. Sivaprasad, An Overview on Constitutive Modelling to Predict Elevated Temperature Flow Behaviour of Fast Reactor Structural Materials, *Trans. Indian Inst. Met.*, 2010, **63**, p 823–831. <https://doi.org/10.1007/s12666-010-0126-6>
32. L. Yumeng, L. Jinxu, L. Shukui, and C. Xingwang, Effect of Hot-rolling Temperature on Microstructure and Dynamic Mechanical Properties of Ti-6Al-4V Alloy, *Rare Metal Mater. Eng.*, 2018, **47**(5), p 1333–1340.
33. Y.C. Lin, J. Huang, D.G. He, X.Y. Zhang, Q. Wu, L.H. Wang, C. Chen, and K.C. Zhou, Phase Transformation and Dynamic Recrystallization Behaviors in a Ti55511 Titanium Alloy during Hot Compression, *J. Alloys Compd.*, 2019, **795**, p 471–482.
34. Y.Q. Jianga, Y.C. Lin, X.Y. Jianga, D.G. Hea, X.Y. Zhanga, and N. Kotkunde, Hot Tensile Properties, Microstructure Evolution and Fracture Mechanisms of Ti-6Al-4V Alloy with Initial Coarse Equiaxed Phases, *Mater. Charact.*, 2020, **163**, p 110272.

Publisher's Note Springer Nature remains neutral with regard to jurisdictional claims in published maps and institutional affiliations.

Springer Nature or its licensor (e.g. a society or other partner) holds exclusive rights to this article under a publishing agreement with the author(s) or other rightsholder(s); author self-archiving of the accepted manuscript version of this article is solely governed by the terms of such publishing agreement and applicable law.